



# Electrocatalytic activity and stability of niobium-doped titanium oxide supported platinum catalyst for polymer electrolyte membrane fuel cells

Sheng-Yang Huang, Prabhu Ganesan, Branko N. Popov\*

Center for Electrochemical Engineering, Department of Chemical Engineering, University of South Carolina, Columbia, SC 29208, USA

## ARTICLE INFO

### Article history:

Received 8 September 2009

Received in revised form 1 February 2010

Accepted 9 February 2010

Available online 24 February 2010

### Keywords:

Niobium-doped titanium oxide

Metal oxide

Cathode catalyst support

Corrosion resistance

Oxygen reduction reaction

Proton exchange membrane fuel cell

## ABSTRACT

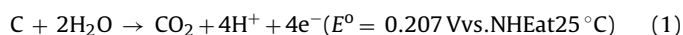
Rutile phase niobium-doped titanium oxide [ $\text{Nb}_x\text{Ti}_{(1-x)}\text{O}_2$ ,  $x=0.25$ ] with a high electrical conductivity ( $1.11 \text{ S cm}^{-1}$ ) was synthesized and investigated as a cathode catalyst support material for polymer electrolyte membrane fuel cells (PEMFCs). The TEM image of the  $\text{Pt}/\text{Nb}_x\text{Ti}_{(1-x)}\text{O}_2$  catalyst revealed that Pt particles ( $d_{\text{Pt}} = 3\text{--}4 \text{ nm}$ ) were deposited on the  $\text{Nb}_x\text{Ti}_{(1-x)}\text{O}_2$  support using a borohydride reduction method. The  $\text{Pt}/\text{Nb}_x\text{Ti}_{(1-x)}\text{O}_2$  catalyst showed comparable oxygen reduction reaction (ORR) activity to that of a commercial Pt/C catalyst (E-TEK) when tested in rotating ring-disk electrode (RRDE). The results of an accelerated durability test (ADT, continuous cycling between 0.6 and 1.4 V) in RRDE indicated high stability for the  $\text{Pt}/\text{Nb}_x\text{Ti}_{(1-x)}\text{O}_2$  electrocatalysts at high potentials in terms of minimum loss in Pt electrochemical surface area (ECSA). Furthermore, the  $\text{Pt}/\text{Nb}_x\text{Ti}_{(1-x)}\text{O}_2$  showed nearly 10-fold higher ORR activity after potential cycling tests when compared to the Pt/C catalyst ( $1.19$  and  $0.13 \text{ mA cm}^{-2}$  for  $\text{Pt}/\text{Nb}_x\text{Ti}_{(1-x)}\text{O}_2$  and Pt/C, respectively). The Pt/C catalyst showed no activity in fuel cell testing after 1000 cycles due to severe carbon corrosion and subsequent disintegration of the catalyst layer. Conversely, the  $\text{Pt}/\text{Nb}_x\text{Ti}_{(1-x)}\text{O}_2$  catalyst showed only a small voltage loss ( $0.11 \text{ V}$  at  $0.6 \text{ A cm}^{-2}$ ) even after 3000 cycles. Based on the ADT results, the  $\text{Pt}/\text{Nb}_x\text{Ti}_{(1-x)}\text{O}_2$  electrocatalyst synthesized in this investigation offers a new approach to improve the reliability and durability of PEM-based fuel cell cathode catalysts.

© 2010 Elsevier B.V. All rights reserved.

## 1. Introduction

The fuel cell is regarded as a green energy technology for the future. Of several types of fuel cells that are under development today, the polymer electrolyte membrane fuel cell (PEMFC) is emerging as a promising candidate in the portable electronics and automobile industries [1–4]. Supported Pt and Pt alloys have been extensively explored as electrocatalysts for fuel oxidation and oxygen reduction in PEM-based fuel cells [5–8]. In contrast to the early catalyst development for PEMFCs, extensive research has been focused on the improvement of catalyst reliability and durability. It has been shown that several factors can diminish the lifetime of PEMFCs including (1) catalyst dissolution, (2) catalyst particle sintering, (3) membrane thinning, and (4) carbon-support corrosion [9–11]. Carbon (e.g., Vulcan XC-72) is the typical catalyst support material for PEM-based fuel cells due to its large surface area, high electrical conductivity, and well-developed pore structure. During the fuel cell start–stop cycles [12], the potential of the cathode can

reach as high as 1.5 V, causing severe carbon corrosion as indicated by the following reaction [13–15]:



The electrochemical corrosion of the carbon support causes agglomeration and sintering of the Pt catalyst particles, resulting in a decreased electrochemical surface area (ECSA) of the catalyst. Carbon corrosion also leads to electrically isolated Pt particles that are detached from the support. Moreover, it has been found that Pt accelerates the corrosion rate of the carbon support [16,17]. These effects result in a rapid degradation of the Pt catalyst and thus shorten the lifetime of the PEMFC, which is limiting for most of its projected applications. Therefore, more robust non-carbon support materials, such as metal oxides, are needed, especially for automotive applications. However, only a small number of studies have reported the development of alternate catalyst supports for fuel cell applications [18–21].

Titanium dioxide ( $\text{TiO}_2$ ) is a widely used material with a variety of potential applications in photocatalysis, photovoltaics, water splitting, and gas sensors [22–24].  $\text{TiO}_2$  possesses good mechanical resistance and stability in acidic and oxidative environments [25]. These properties recommend consideration of  $\text{TiO}_2$  as an alternative catalyst support. However, its low electrical conductivity prevents its use in fuel cells. Therefore, it is of importance to explore

\* Corresponding author at: Center for Electrochemical Engineering, Department of Chemical Engineering, University of South Carolina, Swearingen Engineering Center, Room No. 2C19, Columbia, SC 29208, USA. Tel.: +1 803 777 7314; fax: +1 803 777 8265.

E-mail address: [popov@cec.sc.edu](mailto:popov@cec.sc.edu) (B.N. Popov).

**Table 1**Physical properties of the  $\text{Nb}_x\text{Ti}_{(1-x)}\text{O}_2$  synthesized in this study.

$T^a$ (°C)	Particle size (nm)	Rutile percentage (%)	Conductivity ( $\text{S cm}^{-1}$ )	BET surface area ( $\text{m}^2 \text{g}^{-1}$ )
25	N/A	N/A	$1.47 \times 10^{-6}$	300
400	8.2(A) <sup>b</sup>	5.0	$1.54 \times 10^{-6}$	165
500	8.9(A)	10.2	$3.99 \times 10^{-6}$	79
600	10.7(A) and 20.0(R) <sup>c</sup>	40.9	$2.00 \times 10^{-5}$	24
700	21.1(R)	93.8	0.83	10
800	27.2(R)	97.8	1.00	3
900	31.9(R)	99.1	1.11	2

<sup>a</sup> Heat treatment temperature.<sup>b</sup> Anatase phase.<sup>c</sup> Rutile phase.

possibilities for synthesizing  $\text{TiO}_2$  with good or moderate electrical conductivity. Different approaches have been reported in the literature to improve the electrical conductivity of  $\text{TiO}_2$  including doping with n-type dopants such as vanadium (V), niobium (Nb), and tantalum (Ta) [26] and heat treatment at high temperatures under a reducing atmosphere [27]. Nb is known to be the most promising dopant since the similarity of the ionic radii of  $\text{Nb}^{5+}$  ( $r = 0.70 \text{ \AA}$ ) and  $\text{Ti}^{4+}$  ( $r = 0.68 \text{ \AA}$ ) results in almost no lattice distortion [28,29].

Niobium-doped titanium oxide [ $\text{Nb}_x\text{Ti}_{(1-x)}\text{O}_2$ ,  $x < 1$ ] has been used as a support to prepare platinum catalyst [ $\text{Pt}/\text{Nb}_x\text{Ti}_{(1-x)}\text{O}_2$ ] for oxygen reduction reaction (ORR) and characterized using rotating ring-disk electrode (RRDE) experiment [30,31]. However, to date, the use of  $\text{Nb}_x\text{Ti}_{(1-x)}\text{O}_2$  as a catalyst support under actual PEMFC operating conditions has not been reported. The objectives of the present investigation were to report the synthesis of a platinum catalyst supported on  $\text{Nb}_x\text{Ti}_{(1-x)}\text{O}_2$ , to demonstrate that the synthesized  $\text{Pt}/\text{Nb}_x\text{Ti}_{(1-x)}\text{O}_2$  catalysts possess excellent activity for oxygen reduction and to show the high stability of the  $\text{Pt}/\text{Nb}_x\text{Ti}_{(1-x)}\text{O}_2$  catalyst under potential cycling experiments in half- and full-cell testing conditions.

## 2. Experimental

### 2.1. Synthesis of niobium-doped titanium oxide and supported platinum catalyst

$\text{Nb}_x\text{Ti}_{(1-x)}\text{O}_2$  (with the targeted atomic ratio of Ti to Nb at 75:25) was synthesized via a template-assisted method in an ethanol medium [32]. In the synthesis, a porous structure of  $\text{Nb}_x\text{Ti}_{(1-x)}\text{O}_2$  was created by hydrolyzing titanium isopropoxide (Alfa Aesar) and niobium ethoxide (Alfa Aesar) in the presence of 1-octadecylamine (Sigma–Aldrich). The resulting white product was aged for 48 h, filtered, washed, and dried at  $80^\circ\text{C}$  in a vacuum oven for 12 h. After drying, the fine powder was subjected to heat treatment in a flowing hydrogen atmosphere at temperatures varying between 400 and  $900^\circ\text{C}$ . The resulting dark blue powder was used as the support for  $\text{Pt}/\text{Nb}_x\text{Ti}_{(1-x)}\text{O}_2$  catalyst synthesis. Table 1 lists the physical properties of the  $\text{Nb}_x\text{Ti}_{(1-x)}\text{O}_2$  samples prepared in this study.

Supported platinum catalyst [33.8 wt.%  $\text{Pt}/\text{Nb}_x\text{Ti}_{(1-x)}\text{O}_2$ ] was prepared by a modified borohydride reduction method. For the preparation of the  $\text{Pt}/\text{Nb}_x\text{Ti}_{(1-x)}\text{O}_2$  catalyst, a solution of  $\text{NaBH}_4$  (Sigma–Aldrich), a deaerated suspension of  $\text{Nb}_x\text{Ti}_{(1-x)}\text{O}_2$  support and sodium dodecyl sulfate (Sigma–Aldrich), and a platinum precursor ( $\text{H}_2\text{PtCl}_6$ , Sigma–Aldrich) were prepared separately. The resulting three solutions were immediately mixed together and then stirred for 4 h to allow the adsorption of the colloidal Pt particles onto the  $\text{Nb}_x\text{Ti}_{(1-x)}\text{O}_2$  support. The resulting electrocatalyst ( $\text{Pt}/\text{Nb}_x\text{Ti}_{(1-x)}\text{O}_2$ ) was filtered and dried at  $80^\circ\text{C}$  for 24 h. Finally, the electrocatalyst thus obtained was heated in a tube furnace at  $200^\circ\text{C}$  for 2 h under an argon atmosphere to increase the interaction between Pt particles and the  $\text{Nb}_x\text{Ti}_{(1-x)}\text{O}_2$  support.

### 2.2. Material characterization

Physical properties of the  $\text{Nb}_x\text{Ti}_{(1-x)}\text{O}_2$  and supported Pt catalyst were characterized by BET surface area analysis, X-ray diffraction (XRD), scanning electron microscopy (SEM), and transmission electron microscopy (TEM). BET surface area measurements were performed using a Quantachrome NOVA 2000 BET analyzer. XRD analysis was performed using a Rigaku X-ray diffractometer at  $2\theta$  ranging between  $20^\circ$  and  $80^\circ$  using Copper- $K_\alpha$  radiation. A tube voltage of 30 kV and a current of 15 mA were used during the scanning. TEM was carried out using a JEOL-2100F microscope equipped with a field emission electron gun source and operated at 200 kV. The electrical conductivity of the  $\text{Nb}_x\text{Ti}_{(1-x)}\text{O}_2$  supports was measured at ambient temperature by the conventional four-probe method using pressed pellets [33]. The metal loading of Pt deposited on the  $\text{Nb}_x\text{Ti}_{(1-x)}\text{O}_2$  support was determined by inductively coupled plasma atomic emission spectrometry (ICP-AES). Table 1 lists the  $\text{Nb}_x\text{Ti}_{(1-x)}\text{O}_2$  supports prepared for this study along with their physical characterization results.

### 2.3. Electrochemical characterization

All the electrochemical characterization studies were performed in 0.5 M  $\text{H}_2\text{SO}_4$  using a Pine bipotentiostat (Model AFCBP1), a Pt-wire counter electrode, and an  $\text{Hg}/\text{Hg}_2\text{SO}_4$  reference electrode [0.68 V vs. reversible hydrogen electrode (RHE)]. A rotating ring-disk electrode (RRDE) with a Pt ring and a glassy carbon disk ( $0.247 \text{ cm}^2$ ) was used as the working electrode. The catalyst ink was prepared by blending the catalyst powder [ $\text{Pt}/\text{Nb}_x\text{Ti}_{(1-x)}\text{O}_2$  or  $\text{Pt}/\text{C}$  (20 wt.% Pt on Vulcan XC-72, E-TEK)] with ethanol in an ultrasonic bath. The required amount of the catalyst ink was deposited onto the glassy carbon disk using a micro-pipette. After drying, 5  $\mu\text{L}$  of Nafion solution (0.25 wt.% Nafion) was added on the top of the catalyst layer to ensure better adhesion to the glassy carbon electrode. All the potential values mentioned in the RRDE study are referred to an RHE.

Cyclic voltammograms (CVs) recorded in nitrogen were used to obtain the background capacitive currents and ECSA of the Pt catalysts. The ECSA of Pt was determined by charge integration under the hydrogen desorption peaks appearing between 0 and 0.35 V, which assumes a charge of  $210 \mu\text{C cm}^{-2}$  for the electroactive Pt surface. The electrolyte was purged with oxygen for 30 min prior to the oxygen reduction measurement. The linear sweep voltammograms were recorded at different rotational speeds of the RRDE. The oxygen reduction current was calculated from the difference between currents measured in the nitrogen- and oxygen-saturated electrolytes. The ring potential was maintained at 1.1 V to oxidize the  $\text{H}_2\text{O}_2$  produced in the disk electrode during the ORR.

### 2.4. PEM fuel cell operation

A commercially available catalyzed gas diffusion layer (GDL; LT140EW Low Temperature ELAT<sup>®</sup>GDE Microporous Layer, BASF) was used as the anode for the fuel cell experiments. The anode catalyst loading was  $0.5 \text{ mg}_{\text{Pt}} \text{ cm}^{-2}$ . The cathode catalyst ink was prepared by ultrasonically blending 0.15 g of  $\text{Pt}/\text{Nb}_x\text{Ti}_{(1-x)}\text{O}_2$  or  $\text{Pt}/\text{C}$  catalyst powder (20 wt.% Pt on Vulcan XC-72, E-TEK) with a Nafion solution (5 wt.%, Alfa Aesar) and ethanol for 4 h. The catalyst ink was then sprayed onto a GDL (ELAT LT1400W, BASF). The process was repeated until the desired Pt loading was achieved ( $0.4 \text{ mg}_{\text{Pt}} \text{ cm}^{-2}$  for both  $\text{Pt}/\text{Nb}_x\text{Ti}_{(1-x)}\text{O}_2$  and  $\text{Pt}/\text{C}$ ). The anode and cathode electrodes were hot-pressed onto both sides of a Nafion 112 membrane at  $140^\circ\text{C}$  and 200 psi for 3 min. The MEA was then cooled and assembled in 5 and  $25 \text{ cm}^2$  single cells for performance evaluation and stability studies, respectively.  $\text{H}_2$  and  $\text{O}_2$  humidified

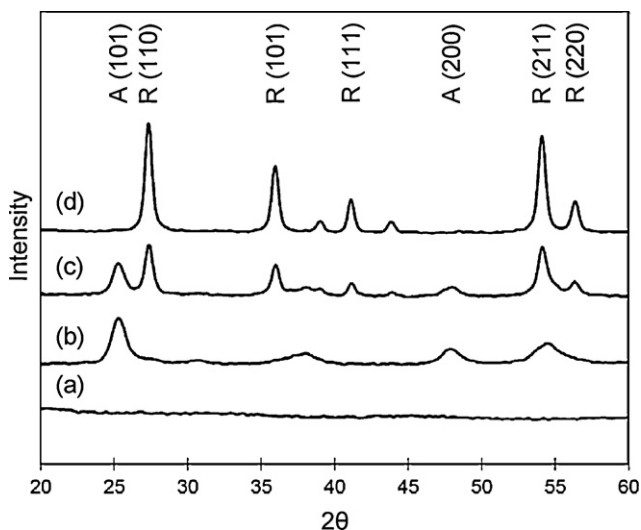


Fig. 1. XRD patterns of  $\text{Nb}_x\text{Ti}_{1-x}\text{O}_2$  subjected to heat treatment at different temperatures: (a) 25 °C; (b) 400–500 °C; (c) 600 °C; (d) 700–900 °C.

at 75 °C were supplied to the anode and cathode compartments, respectively; each at a flow rate of  $150 \text{ mL min}^{-1}$ . Polarization experiments were conducted using a fully automated test station (Fuel Cell Technologies Inc.) at 75 °C.

### 2.5. Accelerated durability tests (ADT)

The electrochemical stability and performance of the  $\text{Pt/Nb}_x\text{Ti}_{1-x}\text{O}_2$  and commercial  $\text{Pt/C}$  cathode catalysts were examined using potential cycling experiments in both half-cell and full-cell conditions. The ADT was performed by continuously cycling the potential between 0.6 and 1.4 V with periodic measurements of ECSA and catalytic activity. Under these conditions, the deterioration of the catalysts was accelerated. Under the half-cell condition, the potential cycling was conducted for 2500 cycles in 0.5 M  $\text{H}_2\text{SO}_4$  at a scan rate of  $50 \text{ mV s}^{-1}$ . Ar gas was bubbled through the electrolyte during potential cycling. The ADT conditions in actual fuel cell operations were carried out in a  $25 \text{ cm}^2$  single cell. The potential cycling experiments were carried out at a scan rate of  $50 \text{ mV s}^{-1}$  with  $\text{H}_2/\text{N}_2$  at a relative humidity (RH) of 100% at both electrodes. The required humidification was achieved by bubbling the reactant gases through water contained in stainless steel bottles held at 80 °C. During fuel cell polarization measurements, the cell temperature was maintained at 80 °C with  $\text{H}_2/\text{air}$  at a backpressure of 25.0 psig. The gas stoichiometry was controlled at 1.2/2.0 for hydrogen and air with respect to the operating current densities. Afterwards, both catalysts were carefully removed from the catalyst layer and subjected to TEM analysis to determine the change in particle size during the ADT. A cross-sectional analysis of the MEA was also investigated using an FEI Quanta 200 Environmental Scanning Electron Microscope.

## 3. Results and discussion

### 3.1. Characterization of $\text{Nb}_x\text{Ti}_{1-x}\text{O}_2$

The influence of the heat treatment temperature on the crystalline phase and particle size of the  $\text{Nb}_x\text{Ti}_{1-x}\text{O}_2$  was investigated using XRD. Fig. 1 compares the XRD patterns of the  $\text{Nb}_x\text{Ti}_{1-x}\text{O}_2$  supports subjected to heat treatment at different temperatures. The freshly prepared  $\text{Nb}_x\text{Ti}_{1-x}\text{O}_2$  powder was amorphous and transformed to crystalline (anatase and rutile phases) upon increasing the heat treatment temperature. A weight loss of ~17% was

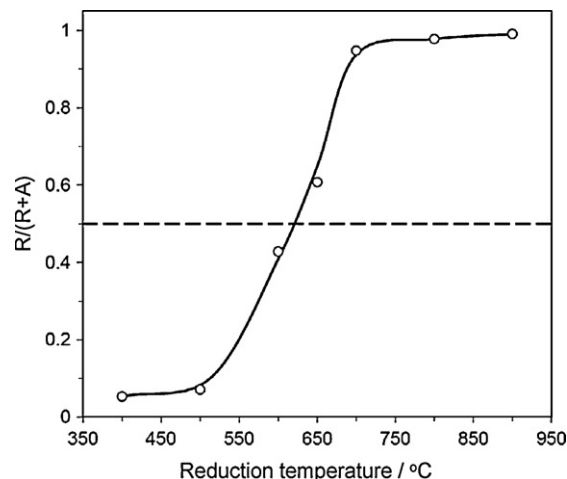


Fig. 2. Anatase-to-rutile transformation with respect to heat-treatment temperature of  $\text{Nb}_x\text{Ti}_{1-x}\text{O}_2$ .

observed at low temperatures (400 and 500 °C) and of ~20% when the  $\text{Nb}_x\text{Ti}_{1-x}\text{O}_2$  was heat-treated at between 600 and 950 °C. It is envisaged from the weight loss that the oxidation states of either or both of Ti and of Nb were reduced to a lower valences. It has widely been believed that the anatase phase is metastable when compared to the rutile. However, at low temperatures, there is only a slight difference between the stability of rutile and the metastable anatase phase [28]. The XRD pattern of  $\text{Nb}_x\text{Ti}_{1-x}\text{O}_2$  heat-treated at 400–500 °C indicates the presence of an anatase phase, as confirmed by the observation of the most intense peak of anatase (1 0 1) at  $2\theta = 25.3^\circ$ . An increase in the rutile phase was observed with respect to the increase in heat treatment temperature, as evidenced by the disappearance of the peak at  $25.3^\circ$  and the appearance of a new peak at  $27.4^\circ$ .

XRD peak intensity ratios were used in order to quantify the degree of the anatase-to-rutile transformation. The ratio between anatase and rutile extracted from XRD spectra was computed using the empirical relationship (Eq. (2)) proposed in the literature [34].

$$R(T) = 0.679 \frac{I_R}{I_R + I_A} + 0.312 \left( \frac{I_R}{I_R + I_A} \right)^2 \quad (2)$$

where  $R(T)$  is the content (in %) of rutile at each heat treatment temperature,  $I_A$  is the intensity of the main (1 0 1) anatase peak, and  $I_R$  is the intensity of the main (1 1 0) rutile peak. The 50% molar anatase and rutile mixture point is marked with a dashed line in Fig. 2. Comparing the results and taking this point to be one of the most characteristic in the anatase-to-rutile transformation, it was found that  $\text{Nb}_x\text{Ti}_{1-x}\text{O}_2$  reached the 50% anatase/rutile point at around 620 °C and became approximately 90% rutile at 700 °C.

The stoichiometric rutile and anatase  $\text{TiO}_2$  are semiconductors with band gaps of 3.0 and 3.2 eV at room temperature, respectively [35]. Nb doping gives rise to shallow donor states [36] 0.02–0.03 eV below the conduction-band minimum and therefore at essentially the same energy as the donor states introduced by oxygen deficiency. Nb is an n-type dopant for  $\text{TiO}_2$  and can be substitutionally incorporated within the rutile lattice to occupy at least 50% of the cation sites. Indeed,  $\text{NbO}_2$  forms a complete range of solid solutions with  $\text{TiO}_2$ . Furthermore, Nb was found incorporated into the  $\text{TiO}_2$  structure because no diffraction peaks for the presence of niobium oxide ( $\text{NbO}_2$  and  $\text{Nb}_2\text{O}_5$ ) or ternary phase  $\text{TiNb}_2\text{O}_7$  were observed in any of the  $\text{Nb}_x\text{Ti}_{1-x}\text{O}_2$  samples.

The effect of heat treatment temperature on the electrical conductivity, shown in Fig. 3a, confirms that the transformation of the oxide material imparted metallic behavior. The conductivity value for the as-prepared  $\text{Nb}_x\text{Ti}_{1-x}\text{O}_2$  was  $1.47 \mu\text{S cm}^{-1}$ , which

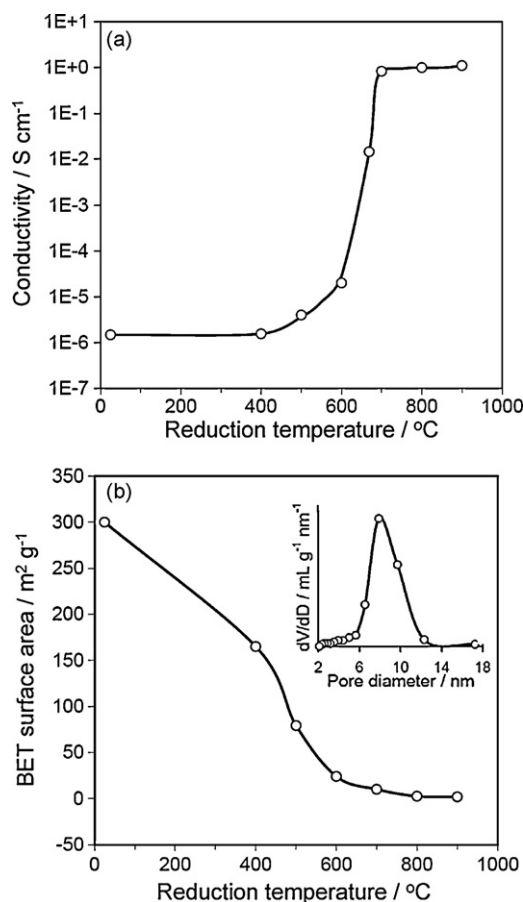


Fig. 3. Effect of heat-treatment temperature on (a) electrical conductivity and (b) BET surface area of  $\text{Nb}_x\text{Ti}_{(1-x)}\text{O}_2$ .

was gradually increased to  $1.11 \text{ S cm}^{-1}$  upon heat treatment at different temperatures under a reducing atmosphere. The structural change had a significant effect on the conductivity of  $\text{Nb}_x\text{Ti}_{(1-x)}\text{O}_2$ . The conductivity of the rutile phase is six orders of magnitude higher than the non-crystalline or anatase phase  $\text{Nb}_x\text{Ti}_{(1-x)}\text{O}_2$ . While the conductivity of  $\text{Nb}_x\text{Ti}_{(1-x)}\text{O}_2$  is less than that of the commercial carbon support (XC-72,  $7.6 \text{ S cm}^{-1}$ ), it is still higher than that recently reported by Chhina et al. [37] for a 10 mol.% Nb-doped titania ( $610 \mu\text{S cm}^{-1}$ ). Such an improvement in the conductivity of  $\text{Nb}_x\text{Ti}_{(1-x)}\text{O}_2$  could be a decisive factor in determining the maximum current density and overall performance of a PEMFC when it is used as a catalyst support.

Fig. 3b presents the BET surface area analysis of  $\text{Nb}_x\text{Ti}_{(1-x)}\text{O}_2$  heat-treated at different temperatures. The surface area decreased from  $300$  to  $2 \text{ m}^2 \text{ g}^{-1}$  when the heat treatment temperature was increased from  $20$  to  $900^\circ\text{C}$  due to the disappearance of mesopores that are present in the fresh,  $400$  and  $500^\circ\text{C}$  heat-treated samples. A sharp decrease in the surface area can be attributed to the anatase-to-rutile phase transformation of  $\text{TiO}_2$  in the presence of the Nb dopant under a reducing atmosphere. However, it has been reported that the phase transformation from anatase to rutile does not occur in Nb-doped  $\text{TiO}_2$  during heat treatment at  $700^\circ\text{C}$  [28]. In our study, the  $\text{Nb}_x\text{Ti}_{(1-x)}\text{O}_2$  heat-treated at  $700^\circ\text{C}$  with the Nb dopant existed exclusively in the rutile phase, with a BET surface area of  $10 \text{ m}^2 \text{ g}^{-1}$ . The surface area (SA) reported here for the conducting  $\text{Nb}_x\text{Ti}_{(1-x)}\text{O}_2$  is much higher than that reported for Magnéli-phase titanium oxides (a mixture of  $\text{Ti}_4\text{O}_7$  and  $\text{Ti}_5\text{O}_9$ ,  $\text{SA} = 1.0 \text{ m}^2 \text{ g}^{-1}$ ),  $\text{Ti}_4\text{O}_7$  ( $2.0 \text{ m}^2 \text{ g}^{-1}$ ) and 10 mol.% Nb-doped titania ( $1.4 \text{ m}^2 \text{ g}^{-1}$ ) [26]. The inserted Barrett–Joyner–Halenda (BJH) pore size distribution for the  $700^\circ\text{C}$  heat-treated  $\text{Nb}_x\text{Ti}_{(1-x)}\text{O}_2$  showed

an average pore size diameter of  $7.9 \text{ nm}$ , indicating the retention of the original mesoporous framework. The  $\text{Nb}_x\text{Ti}_{(1-x)}\text{O}_2$  powder heat-treated at  $700^\circ\text{C}$  was selected for further electrochemical studies due to its optimum electrical conductivity and surface area, which are required for a material serving as a catalyst support for PEMFC applications.

### 3.2. Electrochemical studies

A potential cycling test between  $0.0$  and  $1.4 \text{ V}$  was conducted to examine the electrochemical stability of both the prepared  $\text{Nb}_x\text{Ti}_{(1-x)}\text{O}_2$  and the commercial carbon support (Vulcan XC-72) in an RDE in  $0.5 \text{ M H}_2\text{SO}_4$  with a scan rate of  $50 \text{ mV s}^{-1}$ . An upper potential limit of  $1.4 \text{ V}$  was chosen because (i)  $1.4 \text{ V}$  is the highest potential at which almost no oxygen evolution occurs and (ii)  $1.4 \text{ V}$  is close to the cathode potential in the condition of the reverse current [38] and local fuel starvation [39] at which the corrosion of the carbon support is severe. In the CV plots (Fig. S1), only a double layer charging current was observed for  $\text{Nb}_x\text{Ti}_{(1-x)}\text{O}_2$  indicating its resistance towards oxidation when subjected to high positive potentials. In contrast, the carbon material showed a significant increase in oxidation current at potentials beyond  $0.9 \text{ V}$ . In addition, the large quinone/hydroquinone redox couple at  $\sim 0.55 \text{ V}$  strongly suggested that severe carbon corrosion had occurred during cycling test. The CV results clearly indicated that the  $\text{Nb}_x\text{Ti}_{(1-x)}\text{O}_2$  support is more electrochemically stable compared to the conventional carbon support.

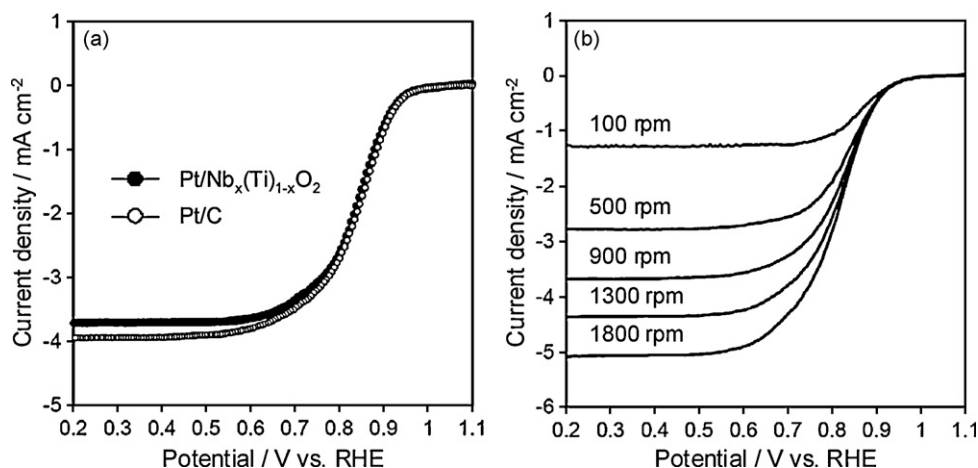
The ORR was studied in oxygen-saturated electrolyte to evaluate the electrocatalytic activity of the  $\text{Pt/Nb}_x\text{Ti}_{(1-x)}\text{O}_2$  electrocatalyst. For the RRDE studies, oxygen within the solution diffused to the surface of the catalyst layer deposited on the glassy carbon electrode and reacted to form water by consuming electrons and producing measurable current. Fig. 4a shows the ORR polarization curves for the  $\text{Pt/Nb}_x\text{Ti}_{(1-x)}\text{O}_2$  and  $\text{Pt/C}$  catalysts. The voltammogram shape for the  $\text{Pt/Nb}_x\text{Ti}_{(1-x)}\text{O}_2$  exhibits very well-defined mass transfer and kinetic regions similar to the one obtained for oxygen reduction on Pt electrodes. The ORR was a under mixed kinetic-diffusion control reaction in the potential region between  $0.95$  and  $0.60 \text{ V}$ , followed by a region where the diffusion limiting current ( $\sim 3.71 \text{ mA cm}^{-2}$ ) was observed. A smaller diffusion current observed for the  $\text{Pt/Nb}_x\text{Ti}_{(1-x)}\text{O}_2$  catalyst can be attributed to the lower surface area of  $\text{Nb}_x\text{Ti}_{(1-x)}\text{O}_2$  ( $10 \text{ m}^2 \text{ g}^{-1}$ ) when compared to Vulcan XC-72 ( $230 \text{ m}^2 \text{ g}^{-1}$ ). Single-step reduction waves with well-developed limiting current plateaus were observed for both  $\text{Pt/Nb}_x\text{Ti}_{(1-x)}\text{O}_2$  and  $\text{Pt/C}$ . The ORR results indicated that the deposited Pt particles provided adequate electron pathway and improved the electrical conductivity of  $\text{Nb}_x\text{Ti}_{(1-x)}\text{O}_2$ .

Fig. 4b shows the polarization curves of the  $\text{Pt/Nb}_x\text{Ti}_{(1-x)}\text{O}_2$  electrocatalysts at various rotational speeds from  $100$  to  $1800 \text{ rpm}$  at a scan rate of  $5 \text{ mV s}^{-1}$ . Well-defined limiting currents were observed as a function of increasing rotation rate. An increase in the rotational speed of the disc electrode resulted in an increase in the limiting current due to the increased availability of oxygen at the electrode surface. First-order kinetics with respect to the oxygen concentration is assumed to determine the number of electrons involved in the ORR. Under such conditions, the current is related to the rotational speed by the Levich–Koutecky equation [40]:

$$\frac{1}{i} = \frac{1}{i_k} + \frac{1}{B\omega^{1/2}} \quad (3)$$

where  $i$  is the current,  $i_k$  is the kinetic current,  $B$  is the Levich slope and  $\omega$  is the rotational speed of the RRDE. The slopes of the Levich–Koutecky plots indicated that the number of electrons involved in the ORR is close to four for the reduction of  $\text{O}_2$  (Fig. S2).





**Fig. 4.** (a) ORR polarization curves for the Pt/Nb<sub>x</sub>Ti<sub>(1-x)</sub>O<sub>2</sub> and Pt/C electrocatalysts recorded at room temperature in an O<sub>2</sub>-saturated 0.5 M H<sub>2</sub>SO<sub>4</sub> solution with a sweep rate of 5 mV s<sup>-1</sup> and a rotation rate of 900 rpm. The Pt loading on each RRDE was 100 μg cm<sup>-2</sup>. (b) Linear sweep voltammograms of Pt/Nb<sub>x</sub>Ti<sub>(1-x)</sub>O<sub>2</sub> for the ORR at various rotational speeds from 100 to 1800 rpm with a sweep rate of 5 mV s<sup>-1</sup>.

Fig. 5a and b shows polarization and power density plots for H<sub>2</sub>-O<sub>2</sub> and H<sub>2</sub>-air fuel cells, respectively, employing Pt/Nb<sub>x</sub>Ti<sub>(1-x)</sub>O<sub>2</sub> cathode electrocatalyst. For the H<sub>2</sub>-O<sub>2</sub> cell, the Pt/Nb<sub>x</sub>Ti<sub>(1-x)</sub>O<sub>2</sub> catalyst generated 1.0 A cm<sup>-2</sup> at 0.60 V and a maximum power density of 0.72 W cm<sup>-2</sup>. A lower performance was obtained for the H<sub>2</sub>-air cell because of the reduced partial pressure of O<sub>2</sub> in air. The current density at 0.6 V was 0.5 A cm<sup>-2</sup>. The maximum peak power density of the H<sub>2</sub>-air cell was 0.33 W cm<sup>-2</sup>, which is approximately half of that generated when employing H<sub>2</sub> and O<sub>2</sub> as the reactants. The polarization

curves demonstrated good ORR kinetics and fuel cell performance for the Pt/Nb<sub>x</sub>Ti<sub>(1-x)</sub>O<sub>2</sub> catalyst synthesized in this study.

### 3.3. Comparison of catalyst stability using accelerated durability test

Fig. 6a and b shows the subset of CVs for the Pt/Nb<sub>x</sub>Ti<sub>(1-x)</sub>O<sub>2</sub> and Pt/C catalysts obtained at room temperature during continuous cycling between 0.6 and 1.4 V for a total of 2500 cycles. The CV curves of Pt/Nb<sub>x</sub>Ti<sub>(1-x)</sub>O<sub>2</sub> in Fig. 6a showed the usual voltammogram for Pt in acid electrolytes and no additional current peak was observed, indicating that the Nb<sub>x</sub>Ti<sub>(1-x)</sub>O<sub>2</sub> support is electrochemically inert and functions as a good electrical conductor under PEMFC operating conditions. Both electrocatalysts exhibited a reduction in the hydrogen under-potential deposition area with repeated potential cycling. This reduction is attributed to the dissolution of Pt and the growth of Pt particles.

The ECSAs of Pt/Nb<sub>x</sub>Ti<sub>(1-x)</sub>O<sub>2</sub> and Pt/C after potential cycling were calculated from the hydrogen desorption peaks shown in Fig. 6a and b and the ECSA, normalized by the initial value, is plotted as a function of cycle number in Fig. 6c. As can be seen from the figure, both the catalysts exhibited a decrease in ECSA with increased cycle numbers. During the CV measurements, these catalysts were exposed to extremely corrosive conditions. By polarizing the catalyst in acidic media, the corrosion of the carbon support resulted in a decrease of the catalyst active surface area due to catalyst particle sintering. Different mechanisms for Pt dissolution and redeposition on the catalyst surface and Pt migration through the surface have been suggested [41] to explain the increase of the catalyst particle size over exposure time. Pt is dissolved into the electrolyte from the supported Pt catalysts and then re-deposited onto the surface of larger particles, a phenomenon known as Ostwald ripening [42]. After 2500 cycles, a huge loss of ECSA (~100%) for the Pt/C catalyst confirmed the corrosion of the high-surface-area carbon support at high positive potentials (>1.0 V) and subsequent processes such as Ostwald ripening, Pt particle migration and sintering (Fig. 6c). In contrast, the small loss of ECSA (~55%) observed for the Pt/Nb<sub>x</sub>Ti<sub>(1-x)</sub>O<sub>2</sub> indicated that it is electrochemically more stable than the Pt/C electrocatalyst. The smaller decrease of ECSA for the Pt/Nb<sub>x</sub>Ti<sub>(1-x)</sub>O<sub>2</sub> electrocatalyst during the potential cycling experiment can be attributed to the stability of the Nb<sub>x</sub>Ti<sub>(1-x)</sub>O<sub>2</sub> support at high positive potentials as discussed in Section 3.2.

Periodic measurement of ORR activity was performed initially and after every 500 cycles during the ADT. Fig. 7 compares the ORR activities in the region between 0.75 and 0.95 V. The activities were

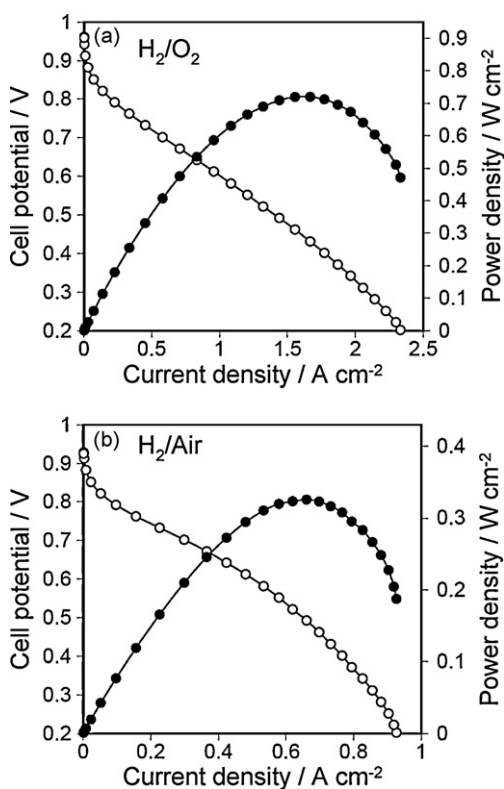


**Fig. 5.** Polarization and power density curves of the PEM fuel cells with the Pt/Nb<sub>x</sub>Ti<sub>(1-x)</sub>O<sub>2</sub> cathode electrocatalysts: (a) H<sub>2</sub>/O<sub>2</sub> and (b) H<sub>2</sub>/air. Measurements were taken at 75 °C with fully humidified reactants (flow rates were 150/150/500 mL min<sup>-1</sup> for H<sub>2</sub>/O<sub>2</sub>/air). Pt loading was controlled at 0.5 mg Pt cm<sup>-2</sup> (LT140EW, BASF) on the anode side and 0.4 mg Pt cm<sup>-2</sup> on the cathode side. No backpressure was applied to the cell during the fuel cell operation.

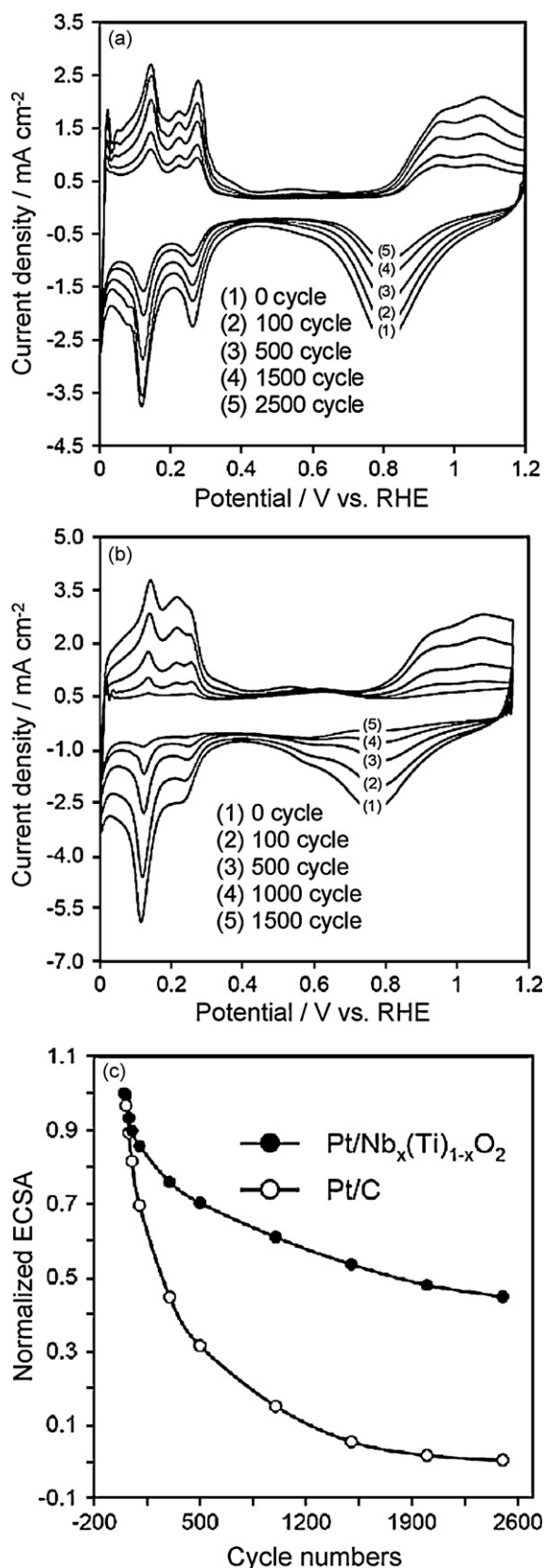


**Fig. 6.** Series of CV plots obtained at room temperature during the ADT experiment on RRDEs: (a) Pt/Nb<sub>x</sub>Ti<sub>(1-x)</sub>O<sub>2</sub> and (b) Pt/C. Cyclic voltammetry was conducted in the potential range between 0.0 and 1.2 V at a scan rate of 50 mV s<sup>-1</sup>. (c) Normalized Pt electrochemical surface area (ECSA) as a function of cycle number for Pt/Nb<sub>x</sub>Ti<sub>(1-x)</sub>O<sub>2</sub> and Pt/C catalysts.

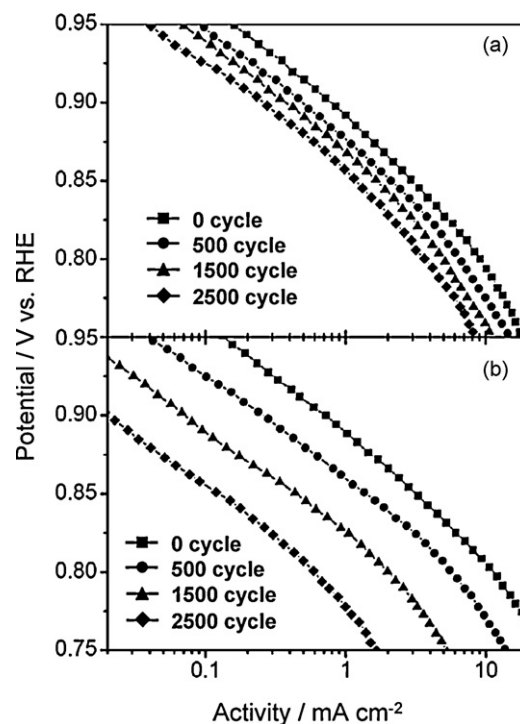


**Fig. 7.** Activities of ORR measurements shown for (a) Pt/Nb<sub>x</sub>Ti<sub>(1-x)</sub>O<sub>2</sub> and (b) Pt/C after different cycle numbers. Data are shown for the positive-moving sweep at 5 mV s<sup>-1</sup> going from 0 to 1.2 V in O<sub>2</sub>-saturated 0.5 M H<sub>2</sub>SO<sub>4</sub> at 900 rpm.

calculated from the experimental data using the mass-transport correction for rotating disk electrodes with the following equations [43]:

$$\frac{1}{i} = \frac{1}{i_k} + \frac{1}{i_d} \quad (4)$$

$$i_k = \frac{i_d i}{i_d - i} \quad (5)$$

where  $i$  is the measured current density during the ORR,  $i_k$  is the mass-transport free kinetic current density, and  $i_d$  is the diffusion-limited current density. Activities ( $A$ ) can be determined by calculating the  $i_k$  using Eq. (5). As can be seen in Fig. 7, the activity of the Pt/Nb<sub>x</sub>Ti<sub>(1-x)</sub>O<sub>2</sub> at 0.85 V (2.97 mA cm<sup>-2</sup>) was similar to that of the Pt/C (3.18 mA cm<sup>-2</sup>). To estimate the effect of the ADT on the oxygen reduction activity, the loss of ORR activity at 0.85 V was calculated using the following equation:

$$\text{ORR}_{\text{loss}}\% = 100 - \frac{A_x}{A_0} \times 100 \quad (6)$$

where  $A_0$  and  $A_x$  are the initial activity and the activity after  $x$  cycles, respectively. Table 2 summarizes the loss of ORR activity at 0.85 V for Pt/Nb<sub>x</sub>Ti<sub>(1-x)</sub>O<sub>2</sub> and Pt/C during potential cycling experiments.

**Table 2**

Activity ( $A$ ) and loss of ORR activity (ORR<sub>loss</sub>) at 0.85 V for Pt/Nb<sub>x</sub>Ti<sub>(1-x)</sub>O<sub>2</sub> and Pt/C measured during potential cycling experiments.

Cycle numbers	Activity (mA cm <sup>-2</sup> )		Loss of ORR activity (%)	
	Pt/Nb <sub>x</sub> Ti <sub>(1-x)</sub> O <sub>2</sub>	Pt/C	Pt/Nb <sub>x</sub> Ti <sub>(1-x)</sub> O <sub>2</sub>	Pt/C
0	2.97	3.18	–	–
100	2.50	2.05	15	35
500	2.11	1.41	28	55
1000	1.80	0.88	39	72
1500	1.67	0.44	43	86
2000	1.37	0.25	54	92
2500	1.19	0.13	59	96

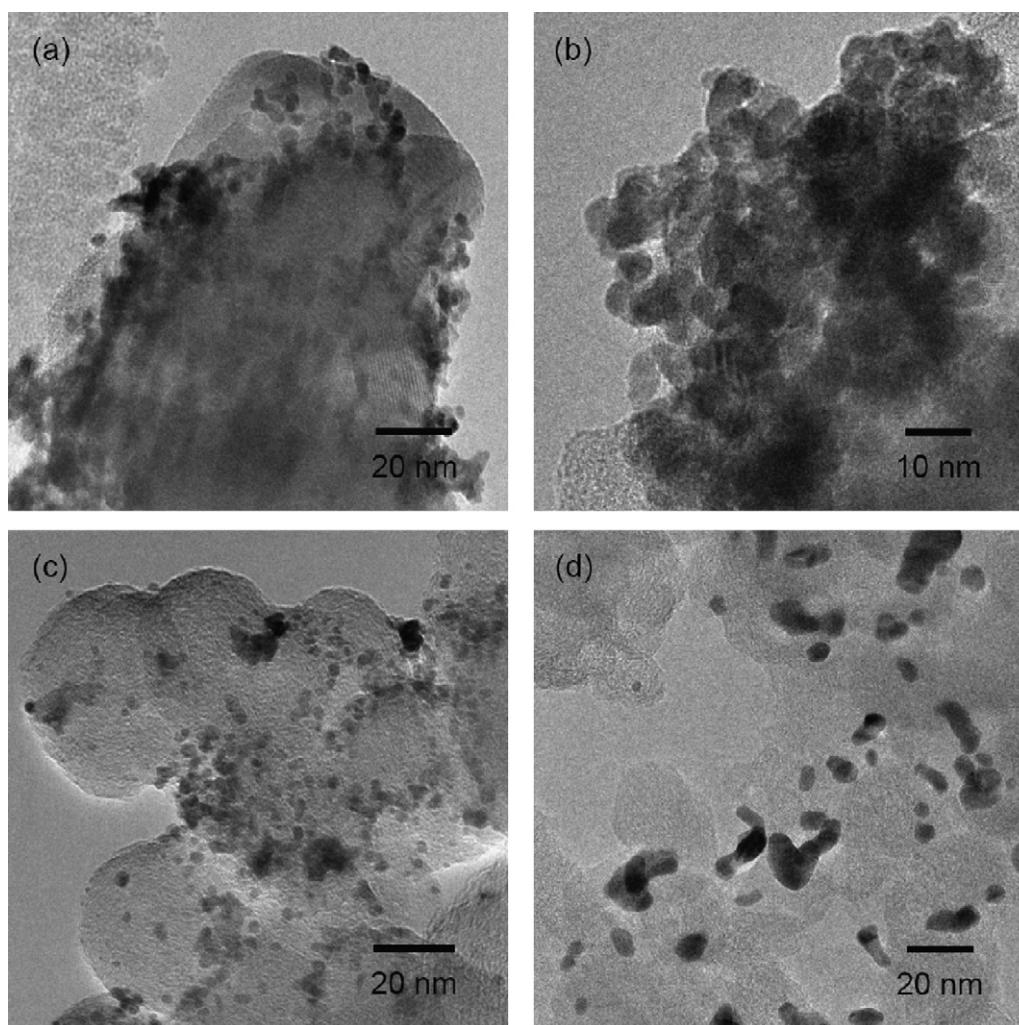


**Fig. 8.** The bright field TEM micrographs of  $\text{Pt}/\text{Nb}_x\text{Ti}_{1-x}\text{O}_2$ : (a) before and (b) after ADT; and of commercial  $\text{Pt}/\text{C}$ : (c) before and (d) after ADT. The potential cycling was conducted for 2500 cycles in 0.5 M  $\text{H}_2\text{SO}_4$  with a scan rate of  $50 \text{ mV s}^{-1}$ .

At the beginning of the ADT, the activity decreased rapidly for the first 500 cycles until it reached a slow but steady decay. As can be seen in the table, the ORR activity of  $\text{Pt}/\text{Nb}_x\text{Ti}_{1-x}\text{O}_2$  was found to be  $1.19 \text{ mA cm}^{-2}$  after 2500 cycles, whereas the  $\text{Pt}/\text{C}$  lost  $\sim 96\%$  of its initial activity (from 3.18 to  $0.13 \text{ mA cm}^{-2}$ ) due to carbon corrosion and subsequent catalyst particles sintering and agglomeration. Additionally, the  $\text{Pt}/\text{Nb}_x\text{Ti}_{1-x}\text{O}_2$  showed nearly 10-fold

higher ORR activity than the  $\text{Pt}/\text{C}$  catalyst after the potential cycling experiment.

**Fig. 8** presents TEM images of  $\text{Pt}/\text{Nb}_x\text{Ti}_{1-x}\text{O}_2$  and  $\text{Pt}/\text{C}$  electrocatalysts before and after the ADT. The TEM image shown in **Fig. 8a** reveals that the deposition of Pt particles onto the  $\text{Nb}_x\text{Ti}_{1-x}\text{O}_2$  support using the borohydride reduction method was successful. In addition, the Pt particles are in the range of 3–4 nm, which is essen-

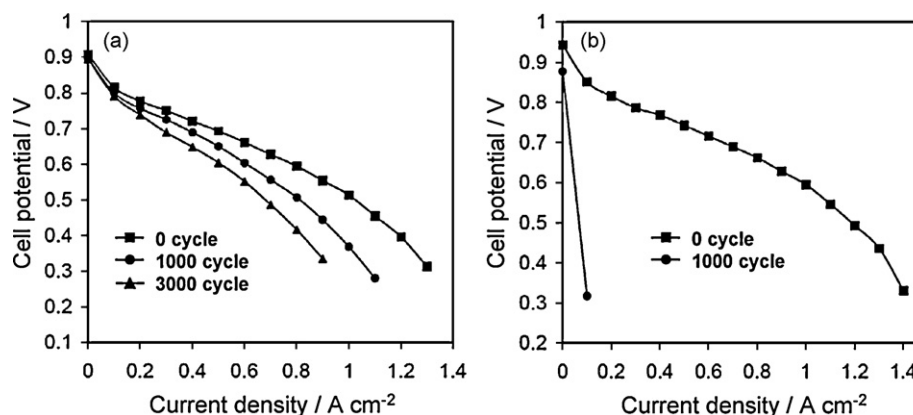


**Fig. 9.** Polarization curves of the PEM fuel cells using (a)  $\text{Pt}/\text{Nb}_x\text{Ti}_{1-x}\text{O}_2$  and (b)  $\text{Pt}/\text{C}$  cathode electrocatalysts after different numbers of cycles.



tial for an electrocatalyst for ORR in PEM-based fuel cells. Fig. 8c exhibits the TEM of well-distributed Pt particles on the carbon support. The average size of the platinum particles ( $d_{\text{Pt}}$ ) was calculated to be between 2 and 3 nm. The Pt particle size in the Pt/C catalyst increased from 2–3 to 7–15 nm after the potential cycling (Fig. 8c and d). The increase in Pt particle size confirms the fact that the major cause for the platinum ECSA loss in the Pt/C catalyst was due to Pt nanoparticle ripening and possibly by aggregation resulting from carbon corrosion. In contrast, the slight agglomeration of Pt particles was observed for the Pt/Nb<sub>x</sub>Ti<sub>(1-x)</sub>O<sub>2</sub> after the potential cycling experiments (Fig. 8a and b). XRD was also used to examine the particle size of the Pt catalysts before and after cycling test. However, the presence of strong diffraction peaks of Nb<sub>x</sub>Ti<sub>(1-x)</sub>O<sub>2</sub> affected the Pt particle size measurement.

Fig. 9 represents the polarization curves of the Pt/Nb<sub>x</sub>Ti<sub>(1-x)</sub>O<sub>2</sub> and Pt/C electrocatalysts in a single cell before and after potential cycling. The effects of potential cycling on cell performance were negligible in the case of the Pt/Nb<sub>x</sub>Ti<sub>(1-x)</sub>O<sub>2</sub> electrocatalyst. A slight decrease in cell voltage (0.11 V) at 0.6 A cm<sup>-2</sup> was observed after 3000 cycles. However, the Pt/C exhibited a large voltage drop after 1000 cycles due to carbon corrosion and subsequent detachment and agglomeration of catalyst particles. The electrochemical corrosion of the carbon surface led to changes in the surface chemistry of the carbon and an increase in the hydrophilicity of the catalyst layer and the GDL, which negatively affected the transport behavior of the reactant gas and water.

The cross-sections of the MEAs, consisting of the Pt/Nb<sub>x</sub>Ti<sub>(1-x)</sub>O<sub>2</sub> or Pt/C cathodes, were characterized by SEM. The Pt/Nb<sub>x</sub>Ti<sub>(1-x)</sub>O<sub>2</sub> electrode retained a similar morphology and catalyst layer thickness (2.3 μm) before and after potential cycling tests. For the Pt/C catalyst layer (Fig. S3a and b), the initial thickness was 16.4 μm, which is approximately seven times higher than the Pt/Nb<sub>x</sub>Ti<sub>(1-x)</sub>O<sub>2</sub> catalyst layer. Cracks were observed in the Pt/C cathode catalyst layer after potential cycling due to the disintegration of the catalyst layer. Carbon corrosion increased the electrode resistance by decreasing the thickness of the catalyst layer, thus reducing the electrical contact with the current collector and significantly decreasing fuel cell performance.

#### 4. Conclusion

In this study, rutile-phase Nb<sub>x</sub>Ti<sub>(1-x)</sub>O<sub>2</sub> with a high electrical conductivity (1.11 S cm<sup>-1</sup>) and high electrochemical stability was synthesized and investigated as an alternate cathode support material for PEMFCs. The TEM image of the Pt/Nb<sub>x</sub>Ti<sub>(1-x)</sub>O<sub>2</sub> revealed that the borohydride reduction method successfully deposited Pt particles ( $d_{\text{Pt}}$  = 3–4 nm) onto the Nb<sub>x</sub>Ti<sub>(1-x)</sub>O<sub>2</sub> support. The Pt/Nb<sub>x</sub>Ti<sub>(1-x)</sub>O<sub>2</sub> catalyst showed ORR activity comparable to a conventional Pt/C catalyst (E-TEK) in RRDE studies. The half-cell ADT results demonstrated high stability and catalytic activity for the Pt/Nb<sub>x</sub>Ti<sub>(1-x)</sub>O<sub>2</sub> electrocatalysts. The Pt/Nb<sub>x</sub>Ti<sub>(1-x)</sub>O<sub>2</sub> showed nearly 10-fold higher ORR activity when compared to the Pt/C after the potential cycling experiment. Fuel cell testing showed no activity for the Pt/C catalyst after 1000 cycles due to severe carbon corrosion and subsequent disintegration of the catalyst layer. Conversely, the Pt/Nb<sub>x</sub>Ti<sub>(1-x)</sub>O<sub>2</sub>-based MEA showed only a small voltage loss (0.11 V at 0.6 A cm<sup>-2</sup>) even after 3000 cycles. The ADT results demonstrated that the Pt/Nb<sub>x</sub>Ti<sub>(1-x)</sub>O<sub>2</sub> electrocatalyst synthesized in this investigation offers a new approach to improve the durability of PEM-based fuel cell cathode catalysts.

#### Acknowledgement

The financial support of NASA-EPSCoR is gratefully acknowledged.

#### Appendix A. Supplementary data

Supplementary data associated with this article can be found, in the online version, at doi:10.1016/j.apcatb.2010.02.025.

#### References

- [1] R. Borup, J. Meyers, B. Pivovar, Y.S. Kim, R. Mukundan, N. Garland, D. Myers, M. Wilson, F. Garzon, D. Wood, P. Zelenay, K. More, K. Stroh, T. Zawodzinski, J. Boncella, J.E. McGrath, M. Inaba, K. Miyatake, M. Hori, K. Ota, Z. Ogumi, S. Miyata, A. Nishikata, Z. Siroma, Y. Uchimoto, K. Yasuda, K.I. Kimijima, N. Iwashita, *Chem. Rev.* 107 (2007) 3904–3951.
- [2] W. Lubitz, W. Tumas, *Chem. Rev.* 107 (2007) 3900–3903.
- [3] H.A. Gasteiger, S.S. Kocha, B. Sompalli, F.T. Wagner, *Appl. Catal. B* 56 (2005) 9–35.
- [4] S.Y. Huang, S.M. Chang, C.T. Yeh, *J. Phys. Chem. B* 110 (2006) 234–239.
- [5] H.R. Colon-Mercado, H. Kim, B.N. Popov, *Electrochem. Commun.* 6 (2004) 795–799.
- [6] S.Y. Huang, S.M. Chang, C.L. Lin, C.H. Chen, C.T. Yeh, *J. Phys. Chem. B* 110 (2006) 23300–23305.
- [7] S.Y. Huang, C.M. Chang, C.T. Yeh, *J. Catal.* 241 (2006) 400–406.
- [8] P.H. Matter, L. Zhang, U.S. Ozkan, *J. Catal.* 239 (2006) 83–96.
- [9] S.G. Chalk, J.E. Miller, *J. Power Sources* 159 (2006) 73–80.
- [10] M.S. Wilson, F.H. Garzon, K.E. Sickafus, S. Gottesfeld, *J. Electrochem. Soc.* 140 (1993) 2872–2877.
- [11] Z. Siroma, K. Ishii, K. Yasuda, Y. Miyazaki, M. Inaba, A. Tasaka, *Electrochem. Commun.* 7 (2005) 1153–1156.
- [12] H. Tang, Z.G. Qi, M. Ramani, J.F. Elter, *J. Power Sources* 158 (2006) 1306–1312.
- [13] K. Kinoshita, *Carbon: Electrochemical and Physicochemical Properties*, John Wiley & Sons, New York, 1988.
- [14] K. Kinoshita, J.A.S. Bett, *Carbon* 11 (1973) 403–411.
- [15] S.I. Pyun, E.J. Lee, T.Y. Kim, S.J. Lee, Y.G. Ryu, C.S. Kim, *Carbon* 32 (1994) 155–159.
- [16] P.J. Ferreira, G.J. Ia O, Y. Shao-Horn, D. Morgan, R. Makharia, S. Kocha, H.A. Gasteiger, *J. Electrochem. Soc.* 152 (2005) A2256–A2271.
- [17] Y.Y. Shao, G.P. Yin, Y.Z. Gao, *J. Power Sources* 171 (2007) 558–566.
- [18] K.S. Lee, I.S. Park, Y.H. Cho, D.S. Jung, N. Jung, H.Y. Park, Y.E. Sung, *J. Catal.* 258 (2008) 143–152.
- [19] T. Ioroi, Z. Siroma, N. Fujiwara, S. Yamazaki, K. Yasuda, *Electrochem. Commun.* 7 (2005) 183–188.
- [20] H. Chhina, S. Campbell, O. Kesler, *J. Power Sources* 161 (2006) 893–900.
- [21] S.Y. Huang, P. Ganesan, S. Park, B.N. Popov, *J. Am. Chem. Soc.* 131 (2009) 13898–13899.
- [22] X. Chen, S.S. Mao, *Chem. Rev.* 107 (2007) 2891–2959.
- [23] D.S. Kim, S.Y. Kwak, *Appl. Catal. A* 323 (2007) 110–118.
- [24] U. Diebold, *Surf. Sci. Rep.* 48 (2003) 53–229.
- [25] Z. Liu, J. Zhang, B. Han, J. Du, T. Mu, Y. Wang, Z. Sun, *Micropor. Mesopor. Mater.* 81 (2005) 169–174.
- [26] D. Morris, Y. Dou, J. Rebane, C.E.J. Mitchell, R.G. Egddell, D.S.L. Law, A. Vittadini, M. Casarin, *Phys. Rev. B* 61 (2000) 13445–13457.
- [27] L.R. Sheppard, T. Bak, J. Nowotny, M.K. Nowotny, *Int. J. Hydrogen Energy* 32 (2007) 2660–2663.
- [28] J. Arbiol, J. Cerdà, G. Dezanneau, A. Cirera, F. Peiro, A. Cornet, J.R. Morante, *J. Appl. Phys.* 92 (2002) 853–861.
- [29] A. Bernasik, M. Radecka, M. Rekas, M. Sloma, *Appl. Surf. Sci.* 65 (6) (1993) 240–245.
- [30] K.W. Park, K.S. Seol, *Electrochem. Commun.* 9 (2007) 2256–2260.
- [31] G.Y. Chen, S.R. Bare, T.E. Mallouk, *J. Electrochem. Soc.* 149 (2002) A1092–A1099.
- [32] B.L. Garcia, R. Fuentes, J.W. Weidner, *Electrochem. Solid-State Lett.* 10 (2007) B108–B110.
- [33] J. Jang, J. Bae, *Sens. Actuators B* 122 (2007) 7–13.
- [34] L.E. Depero, L. Sangaletti, B. Allieri, E. Bontempi, R. Salari, M. Zocchi, C. Casale, M. Notaro, *J. Mater. Res.* 13 (1998) 1644–1649.
- [35] M. Gratzel, *Nature* 414 (2001) 338–344.
- [36] J.W. DeFord, O.W. Johnson, *J. Appl. Phys.* 54 (1983) 889–897.
- [37] H. Chhina, D. Susac, S. Campbell, O. Kesler, *Electrochem. Solid-State Lett.* 12 (2009) B97–B100.
- [38] S.D. Knights, K.M. Colbow, J. St-Pierre, D.P. Wilkinson, *J. Power Sources* 127 (2004) 127–134.
- [39] T.W. Patterson, R.M. Darling, *Electrochem. Solid-State Lett.* 9 (2006) A183–A185.
- [40] H.Y. Jung, S. Park, B.N. Popov, *J. Power Sources* 191 (2009) 357–361.
- [41] H.R. Colon-Mercado, B.N. Popov, *J. Power Sources* 155 (2006) 253–263.
- [42] Z.W. Chen, M. Waje, W.Z. Li, Y.S. Yan, *Angew. Chem. Int. Ed.* 46 (2007) 4060–4063.
- [43] S.L. Gojkovic, S.K. Zecevic, R.F. Savinell, *J. Electrochem. Soc.* 145 (1998) 3713–3720.